Cement and Concrete Composites 134 (2022) 104756

Contents lists available at ScienceDirect

Cement and Concrete Composites

journal homepage: www.elsevier.com/locate/cemconcomp

Experiments and calibration of a bond-slip relation and efficiency factors for textile reinforcement in concrete

Adam Sciegaj [a,b], Fredrik Larsson [c], Karin Lundgren [d,*]

[a] *Department of Mechanics of Materials and Structures, Faculty of Civil and Environmental Engineering, Gdańsk University of Technology, Gdańsk, Poland*
[b] *EkoTech Center, Gdańsk University of Technology, Gdańsk, Poland*
[c] *Department of Industrial and Materials Science, Chalmers University of Technology, Sweden*
[d] *Department of Architecture and Civil Engineering, Chalmers University of Technology, Sweden*

ARTICLE INFO

Keywords:
Carbon textile yarns
Pull-out test
Finite element analysis
Interfilament slip
Bond-slip
Indirect calibration

ABSTRACT

Textile reinforcement yarns consist of many filaments, which can slip relative each other. At modelling of the global structural behaviour, interfilament slip in the yarns, and slip between the yarns and the concrete can be considered by efficiency factors for the stiffness and strength of the yarns, and by applying a bond-slip relation between yarns and concrete. In this work, an effective and robust method for calibration of such models was developed. Two-sided asymmetrical pull-out tests were carried out, with varying embedment lengths designed to obtain both pull-out and rupture of the textile as failure mode. The efficiency factors for strength and stiffness of the textile were very similar, 34% and 35% respectively. This indicates the stress distribution within a yarn to be uneven in a similar manner for small and large stress levels, and that interfilament slip has a larger influence than variation of filaments' strength.

1. Introduction

Textile Reinforced Concrete (TRC) is a promising alternative to other more traditional construction materials and methods, offering the possibility to build corrosion resistant, slender, lightweight, modular, and freeform structures with relatively small environmental impact [1]. TRC resembles fibre reinforced concrete as both include fibres more evenly distributed in the concrete matrix compared to traditionally reinforced concrete structures. However, in TRC, the fibres are bundled and can thus be positioned considering the principal loading direction, which gives more effective use of the fibres. This resembles the use of traditional reinforcement. Thus, TRC combines the benefits of both traditional reinforcement and fibre reinforced concrete [2].

Each textile yarn consists of many continuous fibres (also known as filaments) that are assembled into a yarn during manufacture, [3]. When cast in concrete and loaded, interfilament slip in the yarns, and slip between the yarns and the adjacent concrete takes place [4]. This strongly influences both the crack growth and the ultimate capacity of the TRC, which typically can be caused by rupture of the yarns or anchorage failure. Hegger, Will, Bruckermann and Voss [2] have studied this on the micro-, meso-, and macro levels for uniaxial loading, and suggested a factor for effectiveness of the strength of the textile, to account for the fact that not the whole tensile capacity of the yarns can be used when embedded in concrete. This has been further developed to a design method for bending in Ref. [5], involving an additional coefficient. While an efficiency factor for the strength has been applied by several researchers ([6–9]), only few have applied an efficiency factor for the stiffness [10,11], even though interfilament slip can be expected to influence both stiffness and strength of the yarn.

To be able to follow the crack growth and predict the ultimate capacity of TRC, not only cracking of the concrete itself must be properly addressed, but also the slip and stress transfer between textile reinforcement yarns and concrete. Thus, the stress transfer, commonly called bond, between the textile reinforcement and concrete is vital for the global structural behaviour of the composite [2,12]. This is commonly included in modelling by applying a bond stress versus slip relation [13,14]. To provide input for such models, pull-out tests are commonly carried out. Several test set-ups are used: one-sided [15], or two-sided which are claimed to yield a behaviour more comparable of that of a textile mesh in concrete [16]. Two-sided pull-out tests can have symmetrical [17,18] or unsymmetrical anchoring lengths [16,19]. In these types of tests, the pull-out force and a crack opening are commonly measured. It can be challenging to derive a bond stress versus slip relation from such test results. Analytical solutions for one-sided

---

* Corresponding author.
E-mail addresses: adam.sciegaj@pg.edu.pl (A. Sciegaj), fredrik.larsson@chalmers.se (F. Larsson), karin.lundgren@chalmers.se (K. Lundgren).

https://doi.org/10.1016/j.cemconcomp.2022.104756
Received 1 March 2022; Received in revised form 27 August 2022; Accepted 3 September 2022

pull-out tests can be found in e.g. Ref. [20]. For two-sided symmetrical pull-out tests, Li, Bielak, Hegger and Chudoba [18] have developed an inverse analysis procedure to calibrate a multilinear bond-slip law; however, their calibration procedure can only cope with the ascending part of the behaviour.

The aim of this study was to develop an effective and robust method for testing and calibrating parameters required to model textile reinforced concrete structures. These parameters include efficiency factors for stiffness and strength of the yarn, and the bond-slip relation between yarns and concrete. In this work, two-sided pull-out tests were carried out, and an indirect procedure to calibrate a bond-slip relation and efficiency factors for strength and stiffness of the textile reinforcement in concrete was developed using finite element analyses. By considering pull-out tests with varying embedment length, the calibrated model can be validated for a wide range of (local) loading situations.

The remainder of the paper is structured as follows: Section 2 describes the experimental setup and the main results from the pull-out tests. Section 3 introduces constitutive modelling and the finite element simulations of the experiments and Section 4 describes the indirect calibration procedure for minimising the discrepancy between simulation and test data. In Section 5, the results of the calibration procedure and its validation are presented. Finally, conclusions and an outlook to future work is presented in Section 6.

2. Pull-out tests

2.1. Specimens, test set-up and procedure

In this work, two-sided asymmetrical pull-out tests with varying embedment lengths were carried out. The basis for the choice of two-sided tests was the requirement of the yarn to be embedded in concrete on both sides of the notch to enable calibration of the efficiency factors for stiffness and strength of the yarn. Further, the basis for the choice of an asymmetric embedment length was that it eases both the testing and calibration procedure to have the pull-out failure defined on one of the sides on beforehand. The embedment length varied between 50, 75, and 150 mm nominally, and three tests with each length were carried out. The embedment lengths were chosen to obtain a variation in failure mode, *i.e.,* to investigate both pull-out and rupture of the textile. The specimens were 600 × 100 × 8 mm^3 large, with a textile mesh placed so that one yarn was centrally placed along the length of the specimen, Fig. 1. As can be seen, there were three yarns along the length of the specimens, but only the central yarn was loaded in pull-out at testing. At production, the reinforcement mesh was kept in place by a wooden framework. Saw cuts, 3 mm wide, pre-defined a crack in a notched cross-section, and a drilled hole defined the embedment length of the tested yarn. Individual measurements varied slightly among the specimens, see Table 1.

The test setup used was similar to the one developed by Lorenz and Ortlepp [16] and used by Williams Portal, Fernandez Perez, Nyholm Thrane and Lundgren [19], and it also shares major similarities with the uniaxial tensile test recommendations by RILEM TC 232-TDT [21]. As can be seen in Fig. 1, clamps were placed at the ends of the specimens, thus avoiding applying pressure in the tested embedment length. The clamps were allowed to rotate, to avoid applying bending moment. Rubber sheets were used between the steel clamps and the concrete surface. The bolts were tightened by hand to a level sufficient to avoid slip in the clamps during testing yet avoiding crushing of the concrete at the clamps.

At testing, load was applied by controlling the deformation between the clamps to a rate of 1.2 mm/min. Displacements and crack openings were captured with digital image correlation (DIC), using an ARAMIS adjustable stereo camera system [22]. Images of the tests were acquired with a frequency of 4 Hz, after maximum load this was decreased to 1 Hz. The surface of the specimens was painted in white, and subsequently, black paint applied with a brush generated random pattern that allowed the acquisition of geometrical data. The results were subsequently processed by using the software GOM Correlate [23]. At evaluation of the test results, the crack opening was evaluated as the average deformation difference over the notched section from two predefined measurement points (visible in Fig. 2b) on each side of the notch.

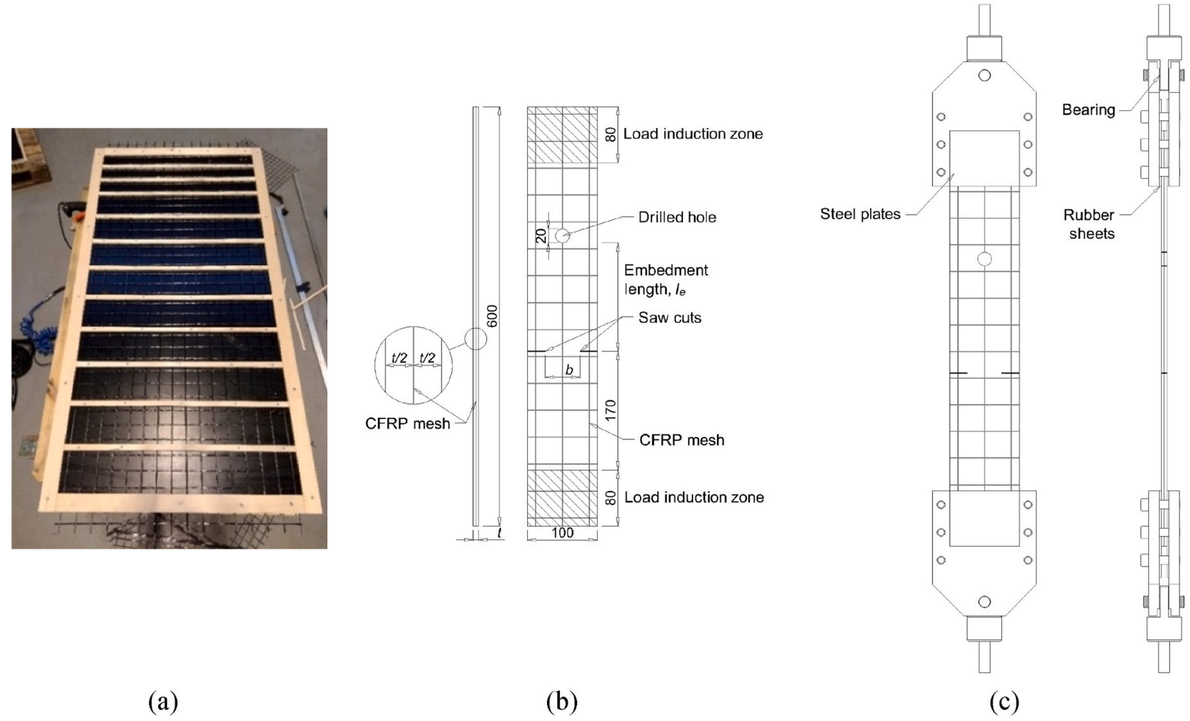

Fig. 1. Pull-out tests; (a) Formwork with textile reinforcement mesh before casting (b) Drawing of specimens; measurements in mm; (c) Test set-up.

Table 1
Overview of pull-out test individual measurements and results. Notations: t - concrete thickness (Fig. 1), b - width at notched cross-section (Fig. 1), l_e - embedment length (Fig. 1), $P_{\max,ru}$ - maximum load at rupture of yarn, $P_{\max,\,po}$ - maximum load at pull-out failure.

Test	t [mm]	b [mm]	l_e [mm]	$P_{\max,ru}$ [N]	$P_{\max,\,po}$ [N]	$P_{\max,\,po}/l_e$ [N/mm]	Failure mode, comments
P150a	7.2	32	150	1894	–		Rupture of the yarn
P150b	8.1	35	145	1827	–		Rupture of the yarn
P150c	7.7	33	153	1913	–		Rupture of the yarn
P75a	7.6	31	79	–	1555	19.7	Pull-out failure
P75b	8.7	32	75/17	1766	(202)	(11.9)	Rupture of the yarn
P75c	7.3	32	79	1827	–		Rupture of the yarn
P50a	7.3	54	43	–	768	17.9	Pull-out failure
P50b	8.2	38	55	–	1347	24.5	Pull-out failure
P50c	7.4	34	55	–	1350	24.5	Pull-out failure
Average				1845		21.6	Pull-out of P75b disregarded
Standard deviation				59		3.4	

3. Materials

The concrete was cast using a commercial concrete mix, type StoCrete R 40. It contained cement of class CEM 1, and had a maximum grain size of 3 mm. The average uniaxial compressive strength was 67.8 MPa, measured in tests on cylinders according to standard [24].

The textile reinforcement was a carbon mesh of type StoFRP Grid 1000 C 390, with yarns of rectangular cross-section and material parameters listed in Table 2. The textile grid was produced in factory environment in an automated process, aligning the fiber yarns in the desired directions and impregnating them with epoxy resin. The connections to yarns in the transverse direction were very weak and did not contribute to yarn-to-concrete bond.

3.1. Experimental results

The results of the pull-out tests are summarised in Table 1. The pull-out tests with long embedment length failed in rupture of the yarn, while the ones with short embedment lengths failed in pull-out. All specimens cracked at the notch at the first peak load, most also cracked at the sections close to the hole. Of the three tests with intermediate embedment length (75 mm nominal), two failed by rupture of the yarn and one in pull-out. For all specimens failing in pull-out, the yarn looked almost intact afterwards; the former position of the cross-thread was clearly visible.

For the tests failing in pull-out, the load divided by the measured embedment length versus the crack opening are shown in Fig. 2a. All these tests cracked at the notch at the first peak load, and after load increase, a crack along the yarn appeared and pull-out failure took place. In the specimens with 50 mm nominal embedment length, this crack along the yarn appeared along the whole embedment length at the maximum load; while in specimen P75a, this crack started from the crack at the notch at maximum load, and reached the hole at the local peak load at a crack opening (at the notch) about 1.3 mm (Fig. 2b–c). Thus, as splitting of the cover occurred, it can be noted that the concrete cover will influence the measured force versus slip, and in turn the calibrated bond-slip response. It is therefore important that the pull-out specimens have a cover of similar size as will be applied in structures, where the use of calibrated parameters is intended for modelling.

The crack at the notch was often slightly curved; therefore, the embedment length measured from the position where the crack crossed the yarn deviated slightly from the nominal, as listed in Table 1. P50a had smaller notches compared to other specimens, therefore it had

Table 2
Technical specifications of the textile reinforcement, StoFRP Grid 1000 C 390.

Parameter	Value	Comment
Young's modulus, E_0	242 GPa	From manufacturer
Tensile capacity, F_0	5500 N/yarn	From manufacturer
Fracture elongation	17‰	From manufacturer
Density, composite	390 g/m^2	From manufacturer
Density, carbon fibre	231 g/m^2	From manufacturer
Mesh free opening	34 mm	Measured, same in both directions
Yarn width	3.55 (0.46) mm	Measured, average and standard deviation
Yarn thickness	0.385 (0.075) mm	Measured, average and standard deviation

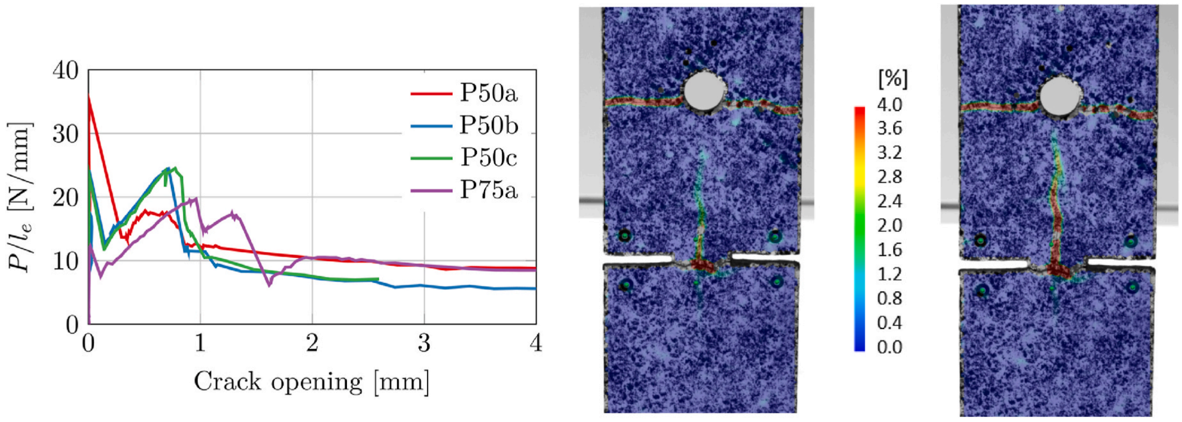

(a) (b) (c)

Fig. 2. Results of tests failing in pull-out. (a) Load divided by measured embedment length versus crack opening at the notch. All these tests cracked at the notch at the first peak load, thereafter pull-out failure took place. (b) and (c) Contours plots of the principal strain, from DIC measurements of specimen P75a. (b) Crack along the yarn started from the notch at maximum load. (c) Crack along the yarn reached the hole at local peak load (crack opening at the notch about 1.3 mm).

higher cracking load and probably its smaller capacity at pull-out can be explained by damages from this higher load.

The load versus crack opening in the tests failing by rupture of the yarn are shown in Fig. 3. In all but one of these tests, rupture of the yarn took place at the notch at the maximum load; the rupture was so brittle that the behaviour couldn't be followed after that. The maximum load at rupture was on average 1845 N (Table 1), which can be compared with the value provided by the manufacturer, 5500 N (Table 2). Thus, the efficiency factor for the strength of the textile in the concrete equalled the ratio between these two values, 34%. In one test, P75b, rupture of the yarn at maximum load took place 17 mm from the notched section, on the side without a drilled hole. The remaining of this test showed a pull-out failure on that side, with a small load capacity.

4. Finite element analyses

4.1. Geometry

To numerically simulate the experiments, all specimens were modelled in nonlinear Finite Element (FE) analyses, using the software DIANA [25]. The specimens were modelled in two-dimensions assuming plane stress, with the thickness of the concrete solid taken according to Table 1. In all analyses, the load induction zones, shaded in Fig. 1, were omitted. This way, the modelled parts of the specimens were 440 mm long and 100 mm wide. For illustration, models of the P50b, P75a, and P150c specimens are shown in Fig. 4. The textile reinforcement mesh was placed as in the experiments; thus, the three vertical yarns were situated symmetrically in the model and the bottom horizontal yarn was located 20 mm from the bottom horizontal edge of the model. The saw cuts and the position of the drilled hole were modelled separately for each specimen, based on the geometry data given in Table 1. Corresponding with the yarn's measured average width and thickness (Table 2), a cross-section area of 1.368 mm^2 and perimeter of 7.872 mm were assigned to each yarn.

4.2. Meshing and boundary conditions

For the concrete solid, quadrilateral linear (4-node) plane stress elements with a side length of 3 mm were used. For the textile reinforcement, 2-node truss elements with the same size were used. Between the materials, interface elements with linear shape functions were generated by the software; thus, interface elements were placed between every yarn and the concrete solid. The finite element meshes for the models of specimens P50b, P75a and P150c are presented in Fig. 5. For clarity, the truss elements are highlighted, and parts of the mesh around the circular hole and the notches are also shown in magnification.

The restraint from the testing machine was simulated by constraining the vertical displacements of all the nodes at the bottom edge, both the concrete plane stress and reinforcement truss elements. Furthermore, rigid body motion was eliminated by constraining the end nodes of the central horizontal yarn in the horizontal direction. The pull-out test was simulated by prescribing a vertical displacement to an auxiliary master node outside of the model; all the nodes on the top boundary of the model (both concrete and textile reinforcement) were tied to this master node (Fig. 4). The use of a master node and tyings simplified the post-processing, as the total force equals the reaction in the master node.

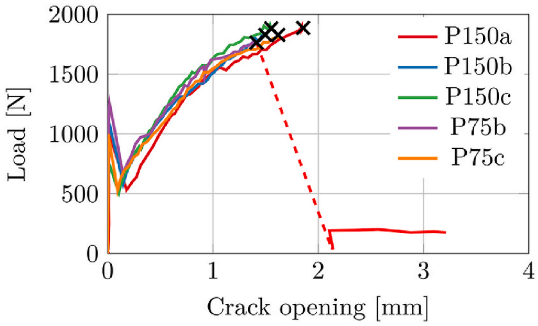

Fig. 3. Load versus crack opening in the pull-out tests failing in rupture of the yarn at maximum load.

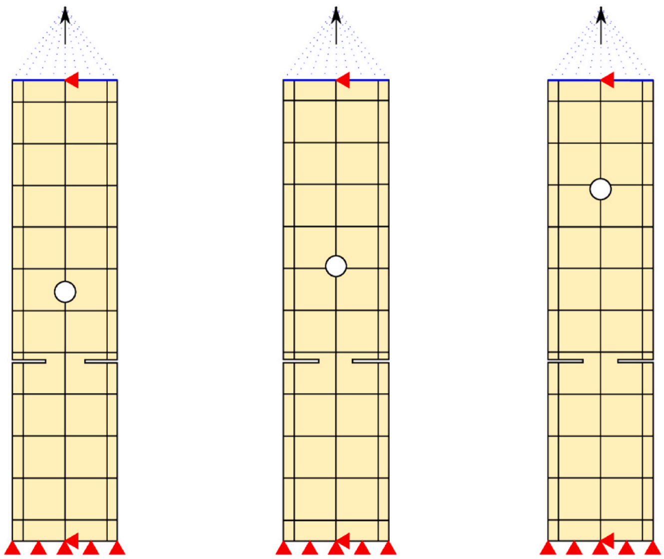

Fig. 4. Geometry and boundary conditions for the finite element models of specimens P50b (left), P75a (centre) and P150c (right). The vertical displacement along the top edge was uniform and controlled by prescribed displacement of the indicated master node (represented by an arrow) tied to the upper edge.

4.3. Material models

For the concrete, the total strain based constative model with a rotating crack orientation was applied. In its most common form, the stress-strain relationships are evaluated in the principal direction of the strain vector. In the general three-dimensional case, the strain vector in the element coordinate system, ε_{xyz} is first transformed to the strain vector in the crack directions, ε_{nst} as

$$\varepsilon_{nst} = \mathbf{T}\varepsilon_{xyz}, \tag{1}$$

where $\mathbf{T}$ is a transformation matrix depending on the current crack orientation. To compute the transformation matrix, the eigenvectors $\mathbf{n}, \mathbf{s}, \mathbf{t}$ of the strain tensor are computed and stored in a rotation matrix $\mathbf{R}$ as

$$\mathbf{R} = [\mathbf{n} \quad \mathbf{s} \quad \mathbf{t}] = \begin{bmatrix} c_{xn} & c_{xs} & c_{xt} \\ c_{yn} & c_{ys} & c_{yt} \\ c_{zn} & c_{zs} & c_{zt} \end{bmatrix}, \tag{2}$$

and the transformation matrix is then computed as

$$\mathbf{T} = \begin{bmatrix} {c_{xn}}^2 & {c_{yn}}^2 & c_{zn}^2 & c_{xn}c_{yn} & c_{yn}c_{zn} & c_{zn}c_{xn} \\ c_{xs}^2 & c_{ys}^2 & c_{zs}^2 & c_{xs}c_{ys} & c_{ys}c_{zs} & c_{zs}c_{xs} \\ c_{xt}^2 & c_{yt}^2 & c_{zt}^2 & c_{xt}c_{yt} & c_{yt}c_{zt} & c_{zt}c_{xt} \\ 2c_{xn}c_{xs} & 2c_{yn}c_{ys} & 2c_{zn}c_{zs} & c_{xn}c_{ys}+c_{yn}c_{xs} & c_{yn}c_{zs}+c_{zn}c_{ys} & c_{zn}c_{xs}+c_{xn}c_{zs} \\ 2c_{xs}c_{xt} & 2c_{ys}c_{yt} & 2c_{zs}c_{zt} & c_{xs}c_{yt}+c_{ys}c_{xt} & c_{ys}c_{zt}+c_{zs}c_{yt} & c_{zs}c_{xt}+c_{xs}c_{zt} \\ 2c_{xt}c_{xn} & 2c_{yt}c_{yn} & 2c_{zt}c_{zn} & c_{xt}c_{yn}+c_{yt}c_{xn} & c_{yt}c_{zn}+c_{zt}c_{yn} & c_{zt}c_{xn}+c_{xt}c_{zn} \end{bmatrix}. \tag{3}$$

Having computed the strain state in the crack-oriented coordinate system, an appropriate constitutive model is used to get the stress vector

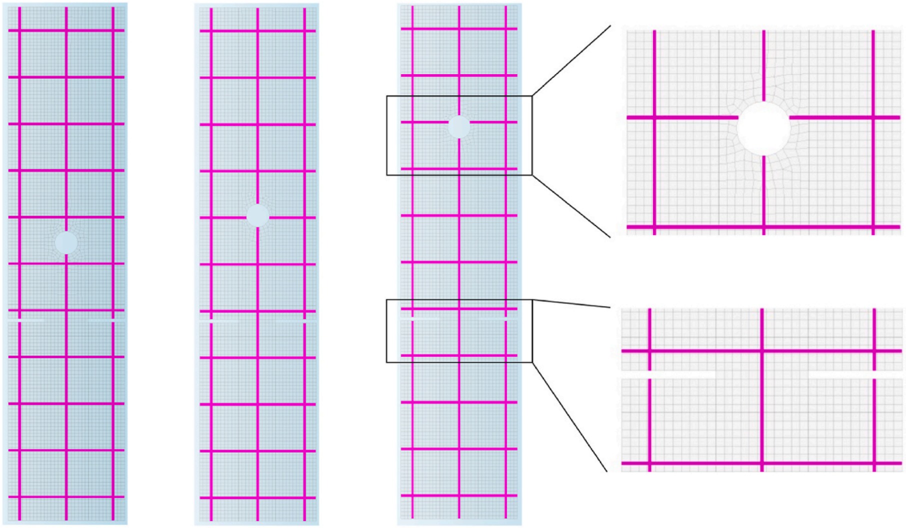

Fig. 5. Finite element meshes for specimens P50b (left), P75a (centre) and P150c (right). Truss elements are highlighted.

in the crack coordinate system:

$$\sigma_{nst} = \sigma(\varepsilon_{nst}), \tag{4}$$

which is later transformed back into the element coordinate system as

$$\sigma_{xyz} = \mathbf{T}\sigma_{nst}. \tag{5}$$

Regarding the material parameters, Young's modulus, tensile strength and fracture energy were computed based on the measured compressive strength, according to Model Code 2010 [26]. In the linear range, the Young's modulus of 40.7 GPa and a Poisson's ratio of 0.2 were specified. The compressive behaviour was simulated using the stress versus strain behaviour suggested by Thorenfeldt [27], where the compressive strength of concrete was given as 67.8 MPa. The constitutive relation in compression can be described with equation

$$\sigma(\varepsilon) = -f_P \frac{\varepsilon}{\varepsilon_P}\left(\frac{n}{n - \left(1 - \left(\frac{\varepsilon}{\varepsilon_P}\right)^{nk}\right)}\right), \tag{6}$$

where f_P and ε_P are the peak stress and strain in compression, respectively. The dimensionless parameters n and k can be calculated as

$$n = 0.80 + \frac{f_{cc}}{17}; \quad k = \begin{cases} 1 & \text{if} \ \ \varepsilon_P \le \varepsilon \le 0 \\ 0.66 + \frac{f_{cc}}{62} & \text{if} \ \ \varepsilon \le \varepsilon_P \end{cases}, \tag{7}$$

where f_{cc} is the cube compressive strength of concrete in MPa.

In tension, a nonlinear tension softening model according to Hordijk et al. [28] was used, with the value of tensile strength and fracture energy given as 4.35 MPa and 156 N/m, respectively. A crack bandwidth equal to the mesh size (3 mm) was assumed (the localisation zone was later verified to take place in one element row). Within the smeared crack formulation, Hordijk tension softening describes the relation between the crack stress, σ_n, and the crack opening, w as follows:

$$\frac{\sigma_n(w)}{f_t} = \begin{cases} \left(1 + \left(c_1 \frac{w}{w_{ult}}\right)^3\right) e^{-c_2 \frac{w}{w_{ult}}} - \frac{w}{w_{ult}}\left(1 + c_1{}^3\right) e^{-c_2} & \text{if} \ \ w < w_{ult} \\ 0 & \text{if} \ \ w \ge w_{ult} \end{cases}, \tag{8}$$

where $c_1 = 3$, and $c_2 = 6.93$. The ultimate crack opening, w_{ult} is linked with the fracture energy, G_F, and tensile strength, f_t as

$$w_{ult} = 5.136 \frac{G_F}{f_t}. \tag{9}$$

For the textile reinforcement, Young's modulus, E_0, was specified to 242 GPa according to Table 2. Uneven stress distribution within the yarn motivated introduction of an efficiency factor for the stiffness, η_E:

$$E = \eta_E E_0 \tag{10}$$

To reproduce rupture of textile reinforcement, the yarn was assumed to rupture when it carried 1845 N, corresponding with the average value of the rupture force in the experiments (Table 1) and an efficiency factor for the strength of $\eta_F = 34\%$. Thus, the capacity of the yarn was set to

$$F = \eta_F F_0 \tag{11}$$

where F_0 is the yarn capacity from manufacturer (Table 2).

For the interface describing the interaction between the yarn and the concrete, it was chosen to apply a one-dimensional bond-slip model. This is commonly considered to be an appropriate level of modelling. However, it can be noted that in this modelling method, splitting of the cover is included in an indirect manner; thus, the calibrated bond-slip relation should depend on the cover. As already mentioned, it is therefore important that the pull-out specimens have a cover of similar size as will be applied in structures, where the use of calibrated parameters is intended for modelling. In this work, a similar bond-slip model as presented for traditional rebars in fib Model Code [26] was used for the interface. The model considers an initially nonlinear development of bond stress upon increasing slip, reaching a plateau at the maximum value of the bond stress. After the plateau, the stress decreases linearly until a final plateau is reached, see Fig. 6. In total, the model formulation requires 7 parameters. Among those, four are slip values s_0 - s_3, and two are bond stress values τ_{max} and τ_f for the maximum and final bond stress, respectively. The last parameter, α, describes the nonlinear growth in the first segment as

$$\tau(s) = \tau_{\max}\left(\frac{s}{s_1}\right)^{\alpha} \tag{12}$$

It is noteworthy, that the parameter s_0 is not included in Ref. [26], and is only internally used in the software implementation. For numerical performance, a linear stiffness of the interface is considered for slip values from 0 up to the initial slip of s_0.

On another note, it is important to point out that the chosen bond-slip model was developed for steel reinforcement being pulled out of concrete, and as such, it considers the mechanical interlock that appears

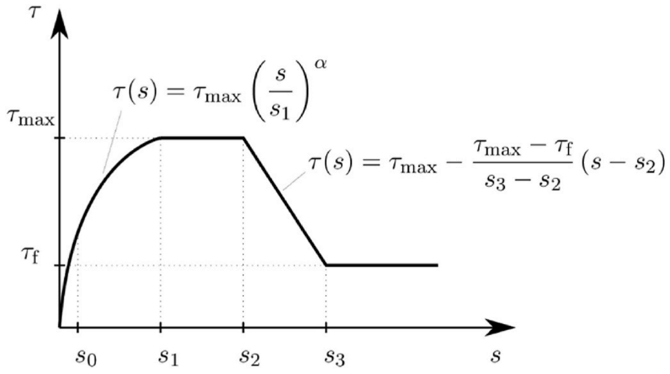

Fig. 6. Bond-slip model from Model Code 2010 [26], with seven parameters: s_0 - s_3, $\tau_{\max}$, τ_{f}, and α.

between reinforcement ribs and the surrounding concrete. The behaviour of textile reinforcement is different, and it was shown (e.g. Ref. [19]) that a multilinear law can approximate the bond-slip model for textile reinforcement very well. However, the Model Code bond-slip model can mimic a multilinear law, with the possibility to have a curved shape in the ascending branch. A further motivation for the choice of this model in this work was its widespread availability in commercial FE codes used in modelling and analysis of engineering structures.

4.4. *Analysis procedure*

The analysis was run in arc-length control, until a prescribed displacement was reached by the master node. For the equilibrium iterations, the Newton-Raphson method was used, and the relative convergence tolerance was set to 0.01 on the iterative displacement increment and out-of-balance force norms. In practice, the simulations were run until failure of convergence, which corresponds to ultimate failure of the specimen. To plot a force versus crack opening graph, the total force was obtained as the vertical reaction force in the master node. Similar as in the evaluation of the experimental results, the crack opening value was computed as an average value of the displacement difference between two nodes on each side of the notch.

5. Calibration procedure

5.1. *Optimisation framework*

The calibration aimed at having one set of parameters in the bond-slip relation (Fig. 6) and efficiency factors for strength and stiffness of the textile reinforcement in concrete to be used in analyses of all specimens. The efficiency factor for the strength of the textile reinforcement was calculated directly from test results as described in Section 2.3, while the remaining parameters were found in a calibration procedure described in the following.

To calibrate the model parameters, an optimisation problem was formulated, minimising the discrepancy between measured experiments and corresponding simulations. To use optimisation for calibration of the parameters, an objective function, which will be minimised in the process, needs to be defined. The parameter set of interest was expressed as

$$\theta = \left\{\tau_{\max}, \tau_f, s_0, s_1, s_2, s_3, \alpha, \eta_E\right\}. \tag{13}$$

After completion of a finite element analysis of a specimen, the resulting force versus crack opening data was extracted. This was compared directly with the experimental relation, and a similarity score was computed. For this problem, the similarity score for specimen i, ε_i, was defined as

$$\varepsilon_i(\theta) = \sqrt{\frac{\sum_{j=1}^{3} \psi_j \int_{w_{j-1}}^{w_j} \left(P_{FEM,i}(\theta; w) - P_{EXP,i}(w)\right)^2 \mathrm{d}w}{\sum_{j=1}^{3} \psi_j \int_{w_{j-1}}^{w_j} \left(P_{EXP,i}(w)\right)^2 \mathrm{d}w}} \tag{14}$$

where $P_{FEM,i}(\boldsymbol{\theta}; w)$ and $P_{EXP,i}(w)$ denote the numerical and experimental external force, respectively, for specimen i as a function of crack opening, w, according to Fig. 7**.** It is noteworthy, that the formulation of $P_{FEM,i}(\boldsymbol{\theta}; w)$ is implicit in the sense that $P_{FEM,i}(w)$ is obtained for a given parameter set θ. The additional hyperparameters ψ_1, ψ_2, and ψ_3 allow for controlling of a relative weight of specific regions in the force-crack opening graph, i.e., from $w = 0$ to w_1, from w_1 to w_2, and from w_2 to w_3.

Combining the similarity score for multiple specimens, the minimisation problem can be expressed in terms of an objective function, $J(\boldsymbol{\theta})$, as follows:

$$\min_{\theta} J(\theta), \quad \text{where} \quad J(\theta) = \frac{1}{|C|}\sum_{i\in C} \varepsilon_i^{2}(\theta) \tag{15}$$

where the set C comprises specimens used for calibration and $|C|$ denotes the dimension of this set. The calibration of the material parameters was thus reduced to finding an optimal set of parameters θ_{opt} which minimised $J(\boldsymbol{\theta})$. For this problem, the Nelder-Mead simplex algorithm [29] was used for optimisation. The advantage of this numerical method is that computing gradient of the objective function $\frac{dJ}{d\theta}$ is not necessary during the iterations.

To minimise the n-dimensional objective function $J(\boldsymbol{\theta})$, the Nelder-Mead algorithm approximates the minimum using a simplex, which is a n-dimensional geometric figure with $n+1$ vertices. First, the value of the objective function is evaluated at all $n+1$ vertices, after which the vertices are ordered according to the value of the function, i.e.,

$$J(\theta_1) \leq J(\theta_2) \leq \ldots \leq J(\theta_{n+1}), \tag{16}$$

where $\{\theta_j\}_{j=1}^{n+1}$ represents the coordinates of the j-th vertex in the n-dimensional space. According to the above ordering, θ_1 and θ_{n+1} are referred to as the best and worst vertices, respectively. In each iteration, the algorithm finds the next approximating simplex with the help of four possible operations: reflect, expand, contract and shrink. The individual steps of one iteration of the algorithm are listed as follows:

- **Sort.** Sort the vertices of the simplex according to Eq. (16) and compute the centroid of the n best vertices

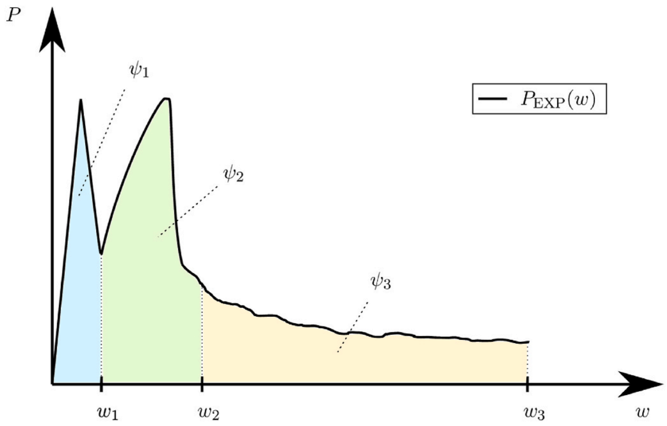

Fig. 7. Force versus crack opening divided in regions by crack openings w_1 and w_2, with weight parameters $\psi_1 - \psi_3$ applied to the different regions. These were used at calculation of the similarity score according to Eq. (14).

$$\overline{\theta} = \frac{1}{n}\sum_{j=1}^{n}\theta_j \tag{17}$$

- **Reflect.** Compute the reflected point θ_r

$$\theta_r = \overline{\theta} + \rho(\overline{\theta} - \theta_{n+1}) \tag{18}$$

Evaluate $J(\theta_r)$. If $J(\theta_1) \leq J(\theta_r) \leq J(\theta_n)$ replace θ_{n+1} with. θ_r.

- **Expand.** If $J(\theta_r) \leq J(\theta_1)$ compute the expanded point θ_e

$$\theta_e = \overline{\theta} + \chi(\theta_r - \overline{\theta}) \tag{19}$$

Evaluate $J(\theta_e)$. If $J(\theta_e) \leq J(\theta_r)$ replace θ_{n+1} with θ_e. Otherwise replace θ_{n+1} with. θ_r.

- Contract:
  a. If $J(\theta_n) \leq J(\theta_r) \leq J(\theta_{n+1})$ compute the outside contracted point

$$\theta_{oc} = \overline{\theta} + \zeta(\theta_r - \overline{\theta}) \tag{20}$$

Evaluate $J(\theta_{oc})$. If $J(\theta_{oc}) \leq J(\theta_r)$ replace θ_{n+1} with θ_{oc}. Otherwise go to Step 5.

$$\theta_{ic} = \overline{\theta} - \zeta(\theta_r - \overline{\theta}) \tag{21}$$

b. If $J(\theta_r) \geq J(\theta_{n+1})$ compute the inside contracted point

Evaluate $J(\theta_{ic})$. If $J(\theta_{ic}) \leq J(\theta_{n+1})$ replace θ_{n+1} with θ_{ic}. Otherwise go to Step 5.

- **Shrink.** Shrink the simplex towards the best vertex. For all $2 \leq j \leq n+1$

$$\theta_j = \theta_1 + \kappa\left(\theta_j - \theta_1\right) \tag{22}$$

The scalar parameters $\rho, \chi, \zeta, \kappa$ control the amount of the reflect, expand, contract, and shrink operations, respectively. In the standard implementation of the Nelder-Mead method, they are chosen as

$$\{\rho, \chi, \zeta, \kappa\} = \{1, \ \ 2, 0.5, 0.5\} \tag{23}$$

The algorithm iterates until convergence is reached, which is usually considered to be the case when the error of the objective function values between iterations falls beneath a preset tolerance. In this work, a value of 0.0001 was chosen. Alternatively, the procedure can be terminated after a preset number of iterations or objective function evaluations.

It is important to emphasize that the overall performance of the algorithms is governed mainly by the time it takes to evaluate the objective function given in Eq. (15). As this is possible only after executing several FE analyses (which can be run in parallel), many variables such as the mesh size and constitutive formulation that affect the performance of the FE solver, will be the decisive factor.

5.2. *Choice of parameters in the calibration procedure*

Values for an initial parameter set were estimated based on the test results using simplified assumptions, such as a constant bond stress over short embedment length. The calibration procedure was carried out in two rounds, mainly characterised by:

Calibration I ($\eta_E = 1$): The efficiency factor for the stiffness, η_E, was set to 1.0, and the set of experiments used for calibration, C, included P50b, P50c and P75a, all failing in pull-out. Hence, the full (theoretical) stiffness of the yarns was assumed, and only the bond-slip relation parameters were calibrated.

Calibration II ($\eta_E \neq 1$): The efficiency factor for the stiffness, η_E, was included in the parameter set θ, alleviating the assumption of full θ, and thus assuming that the full (theoretical) stiffness of the yarns could not be utilised. Further, the set of experiments used for calibration, C, included two specimens failing by rupture of the yarn (P75b and P150a) in addition to the ones included in *Calibration I* (P50b, P50c and P75a).

Details are given in Table 3. It can be noted that the parameters for the similarity score (Fig. 7) were chosen so that focus was placed on the intermediate part of the force versus crack opening curve, as it included gradual pull-out of the yarn and subsequent pull-out failure or rupture. In the first part, cracking at the notch took place, which was governed by cracking of the concrete, and the bond-slip and the stiffness of the yarn had only very minor influence. In the last part, frictional sliding took place after possible pull-out failure, while the tests failing in rupture were very brittle. Further, it can be noted that P50a was not included in any of the sets of experiments used for calibration. This was because its pull-out capacity may have been influenced by damages from its high cracking load, which in turn depended on the smaller notches of this specimen compared to the others.

6. Results and discussion

The calibrated values of the parameter sets are given in Table 3. Results of analyses in *Calibration I ($\eta_E = 1$)* are presented in Fig. 8, both for the specimens included in the calibration set (white background) and the remaining ones used for validation (light-green background). The results are shown for the initial parameter estimate as well as for the calibrated parameter values. As expected, the calibration procedure improved the agreement. The results of the calibrated parameter set agree well with the calibration set, however, the results for the validation set show some discrepancy. Most notably, the stiffness of the global force versus crack opening relation for the P75 and P150 specimens is considerably larger in the analyses than measured in the experiments. This motivated *Calibration II ($\eta_E \neq 1$)*, in which the efficiency factor for the stiffness, η_E, was included in the parameter set.

The resulting force versus crack opening from analyses in *Calibration II ($\eta_E \neq 1$)* are presented in Fig. 9. The modification of the stiffness of the yarn substantially improved the agreement for the specimens failing in rupture, and also slightly improved the already reasonable agreement for specimens failing in pull-out (compare Figs. 8 and 9). However, as can be seen in Fig. 10, the calibrated bond-slip relation varies quite significantly. For *Calibration II ($\eta_E \neq 1$)*, the identified bond-slip relation is much stiffer, while the effective compliance is maintained due to the reduced stiffness of the reinforcement yarn *($\eta_E < 1$)*. As already alluded

Table 3
Parameters in the calibration procedure.

Parameter	Calibration I		Calibration II	
Parameter set θ	$\theta = \{\tau_{max}, \tau_f, s_0, s_1, s_2, s_3, \alpha\}$		$\theta = \{\tau_{max}, \tau_f, s_0, s_1, s_2, s_3, \alpha, \ \eta_E\ \}$	
Calibration set C	$C = \{P50b, \ P50c, \ P75a\}$		$C = \{P50b, \ P50c, P75a, \ P75b, \ P150a\}$	
w_1 [mm]	0.2		0.2	
w_2 [mm]	1.5		1.5[a]	
ψ_1 [−]	0		0	
ψ_2 [−]	1.0		1.0	
ψ_3 [−]	0.2		0.2 or 0[b]	
	Initial values	**Calibrated values**	**Initial values**	**Calibrated values**
τ_{max} [MPa]	2.45	2.588	2.45	2.910
τ_f [MPa]	0.77	0.830	0.77	0.822
s_0 [mm]	0.01	0.115	0.01	0.015
s_1 [mm]	0.30	0.372	0.30	0.025
s_2 [mm]	0.79	0.419	0.79	0.086
s_3 [mm]	1.45	1.336	1.45	1.092
α [−]	0.40	0.316	0.40	0.658
η_E [−]	1.0	1.0[c]	0.40	0.353

[a] was set to 1.5 mm for specimens failing in pull-out in experiments, and to the measured crack opening at rupture for specimens failing in rupture in experiments.

[b] was set to 0.2 for specimens failing in pull-out in experiments, and 0 for specimens failing in rupture in experiments.

[c] Not included in the parameter set.

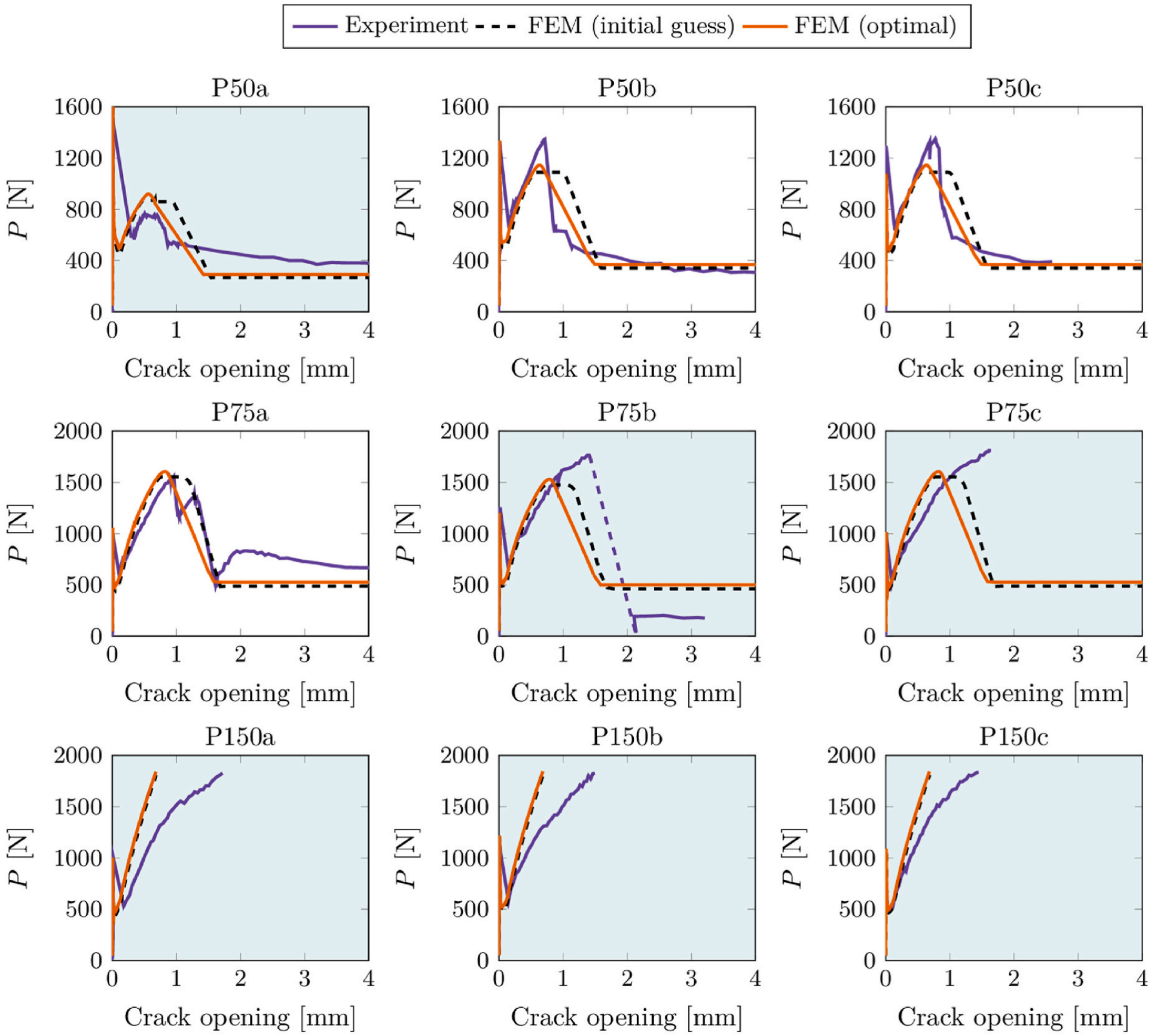

Fig. 8. Results of analyses in Calibration I ($\eta_E = 1$): Force versus crack opening obtained with the initial and calibrated parameter set. Validation set in light-green background. (For interpretation of the references to colour in this figure legend, the reader is referred to the Web version of this article.)

to in Section 3.3, the calibrated bond-slip relation closely resembles a multilinear model, thus a multilinear law might be more suitable for this type of textile reinforcement. At the same time, the results show that the used nonlinear bond-slip model can, with a suitable choice of parameters, mimic a multilinear law with horizontal segments.

Looking at the calibrated values (Table 3), it is noteworthy that the calibrated value of the efficiency factor for stiffness, η_E, was found to be 35%, which agrees very well with the efficiency factor for strength calculated from the test results of 34%. The similarity of these values means that a yarn lost its stiffness and strength to an approximately equal level when cast in concrete. This indicates that the stress distribution within a yarn was uneven in a similar manner for small and large stress levels. Thus, the variation of strength between filaments was of minor importance compared to the interfilament slip. While the efficiency factor for strength has received quite some attention in literature [5,8,9], an efficiency factor for the stiffness is less investigated. Si Larbi, Agbossou and Hamelin [10] used an efficiency factor for the stiffness in analyses of beams strengthened with textile-reinforced concrete, and Rampini, Zani, Colombo and di Prisco [11] included an efficiency factor for the stiffness in equations, but set it to 1.0. To the authors' knowledge, calibrated values for efficiency factors of the strength and stiffness have not been compared before.

Some examples of results from the analyses with calibrated parameters (*Calibration II ($\eta_E \neq 1$)*) can be seen for the P75a specimen in Fig. 11, where bond stress distribution is shown for a portion of the central yarn at different load levels. As soon as the specimen has cracked at the notch, a sharp change in the sign of bond stress can be observed at the location of the crack. The value of the bond stress grows with increasing load, but as shown in the graph, its absolute value never exceeds $\tau_{\max} = \pm 2.91$ MPa. Furthermore, as the external load grows, the portion of the yarn subjected to large bond stresses also grows. The bond distribution before maximum load is symmetric around the notch, but becomes unsymmetric after maximum load is reached, when pull-out failure in the upper part took place. Further, it can be seen that the bond distribution in the part below the crack (where failure did not take place due to the longer embedment length) was influenced by local unloading in this non-critical part. At large slip values, a constant bond stress of $\tau_f = \pm 0.82$ MPa is observed close to the crack.

The objective function value versus number of iterations in the calibration procedure is shown for both calibrations in Fig. 12. For both calibrations, the procedure is robust, reducing the objective function almost monotonically with the iterations. As can be seen, the results converged after about 150 iterations for Calibration I ($\eta_E = 1$), while Calibration II ($\eta_E \neq 1$) required about 250 iterations. The objective function, i.e., the mean square of the similarity score, was reduced from ~3% to ~2% when the richer parameter space in *Calibration II* was used.

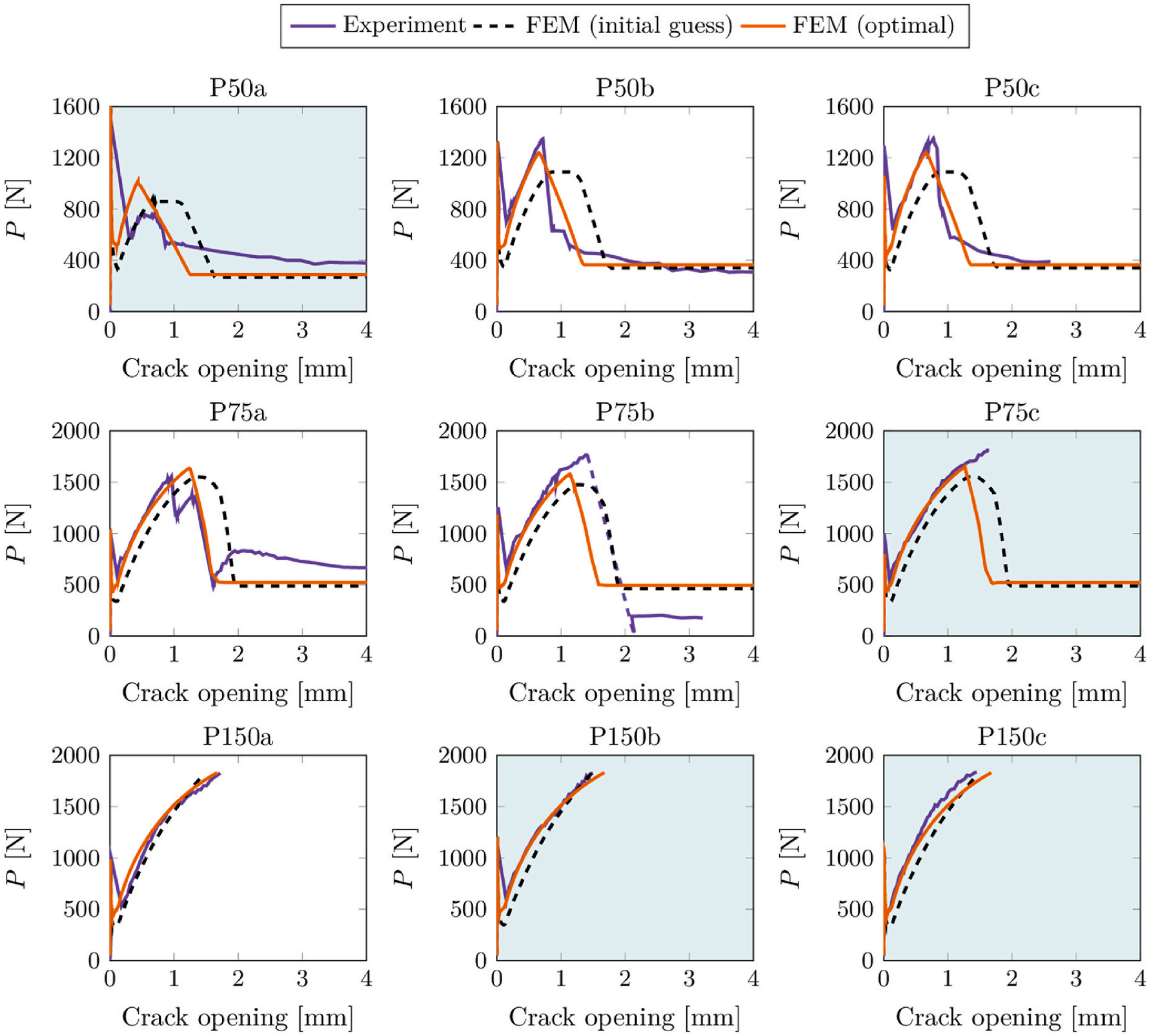

Fig. 9. Results of analyses in Calibration II ($\eta_E \neq 1$): Force versus crack opening obtained with the initial and calibrated parameter set. Validation set in light-green background. (For interpretation of the references to colour in this figure legend, the reader is referred to the Web version of this article.)

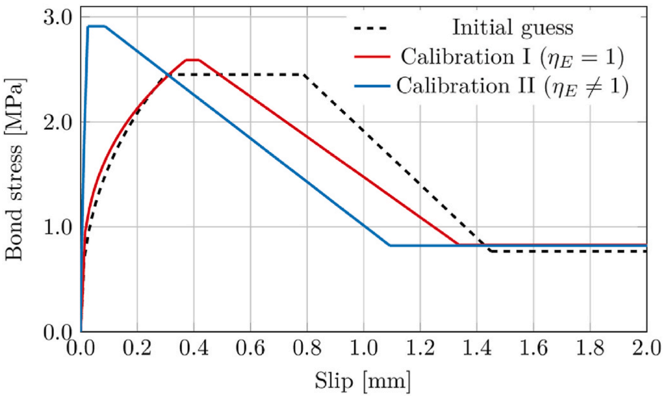

Fig. 10. Bond stress versus slip, results of the calibration procedure.

7. Conclusions and outlook

In this work, two-sided pull-out tests were carried out, with varying embedment lengths designed to obtain both pull-out and rupture of the textile as failure mode. Further, a procedure to calibrate a bond-slip relation and efficiency factors for strength and stiffness of the textile reinforcement in concrete was developed. While the efficiency factor for strength of the textile reinforcement was calculated directly from test results, the other parameters were found in a calibration procedure. The following conclusions can be drawn from the work:

- By designing a series of two-sided asymmetrical pull-out tests with embedment lengths varying to obtain both pull-out and rupture of the textile as failure mode, such a test series provides sufficient information for calibration of parameters required in analyses of the global structural behaviour of textile reinforced concrete structures.
- The indirect calibration procedure, minimising the discrepancy between test data and finite element simulations, was shown to be effective and robust.
- Including an efficiency factor for the stiffness of the yarn substantially improved the agreement between experimental and analysis results for the specimens failing in rupture.
- It is noteworthy that the efficiency factors for strength and stiffness of the textile reinforcement in concrete were very close, 34% and 35% respectively. The numbers as such likely vary for different yarns and concrete, but the similarity between them in this work is interesting. This may indicate that interfilament slip results in uneven stress distribution within a yarn in a similar manner for small and large stress levels, and that the variation of strength between filaments is of minor importance.

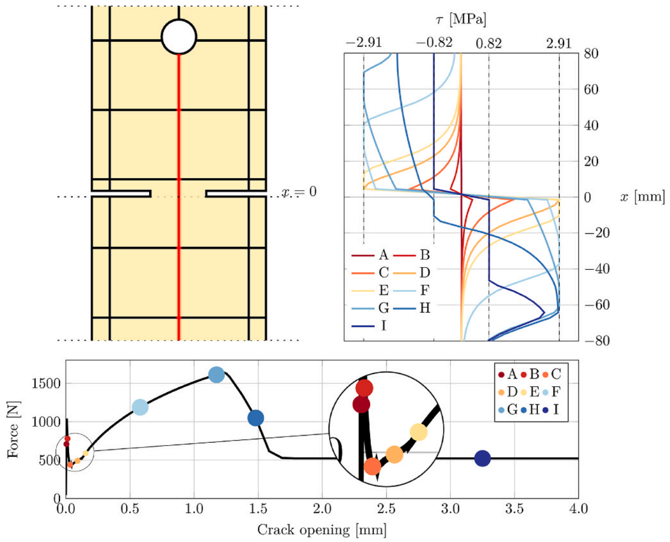

Fig. 11. Bond stress profiles for the P75a specimen along a portion of the central yarn (marked in red) at seven different load levels, denoted A-I, respectively. (For interpretation of the references to colour in this figure legend, the reader is referred to the Web version of this article.)

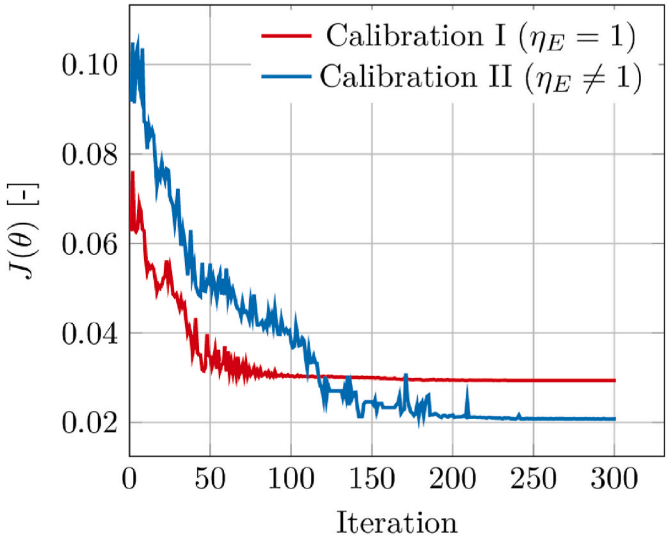

Fig. 12. Objective function value versus iteration number.

As to further work, the calibrated model should be applied in analyses of various textile reinforced concrete structures and compared with experimental results for further validation. Due to the relatively small scale of the textile reinforcement grid (compared to conventional steel reinforcement), multiscale numerical procedures should be developed to analyse large scale structures efficiently, omitting the need to resolve every single yarn.

Declaration of competing interest

The authors declare that they have no known competing financial interests or personal relationships that could have appeared to influence the work reported in this paper.

Data availability

Data will be made available on request.

Acknowledgements

The research was financially supported by the Swedish Research Council (Vetenskapsrådet) under grant 2018-03691. The work regarding numerical modelling and optimisation was financially supported by Gdańsk University of Technology under grant DEC-2/2020/IDUB/I.1 within the NOBELIUM JOINING GUT RESEARCH COMMUNITY programme. StoCrete donated materials used in the experiments. The computations were performed on resources at the Chalmers Centre for Computational Science and Engineering (C3SE) provided by the Swedish National Infrastructure for Computing (SNIC).

References

[1] N.W. Portal, K. Lundgren, H. Wallbaum, K. Malaga, Sustainable potential of textile-reinforced concrete, J. Mater. Civ. Eng. 27 (7) (2015), https://doi.org/10.1061/(ASCE)MT.1943-5533.0001160.

[2] J. Hegger, N. Will, O. Bruckermann, S. Voss, Load-bearing behaviour and simulation of textile reinforced concrete, Materials and Structures/Materiaux et Constructions 39 (292) (2006) 765–776, https://doi.org/10.1617/s11527-005-9039-y.

[3] R. Fangueiro, in: Fibrous and Composite Materials for Civil Engineering Applications, first ed. ed., Woodhead Publishing, 2011.

[4] W.E. Weber, V. Mechtcherine, Modeling the dynamic properties of fibre-reinforced concrete with different coating technologies of multifilament yarns, Cement Concr. Compos. 73 (2016) 257–266, https://doi.org/10.1016/j.cemconcomp.2016.07.017.

[5] J. Hegger, S. Voss, Investigations on the bearing behaviour and application potential of textile reinforced concrete, Eng. Struct. 30 (7) (2008) 2050–2056, https://doi.org/10.1016/j.engstruct.2008.01.006.

[6] M. Lee, J. Mata-Falcón, W. Kaufmann, Load-deformation behaviour of weft-knitted textile reinforced concrete in uniaxial tension, Mater. Struct. 54 (6) (2021) 210, https://doi.org/10.1617/s11527-021-01797-5.

[7] I.G. Colombo, A. Magri, G. Zani, M. Colombo, M. di Prisco, Erratum to: textile Reinforced Concrete: experimental investigation on design parameters, Mater. Struct. 46 (11) (2013) 1953–1971, https://doi.org/10.1617/s11527-013-0023-7.

[8] W. Brameshuber, Textile Reinforced Concrete. State-Of-The-Art Report of RILEM Technical Committee 201-TRC, Rilem Publications S.A.R.L., 2006.

[9] A. Peled, A. Bentur, Geometrical characteristics and efficiency of textile fabrics for reinforcing cement composites, Cement Concr. Res. 30 (5) (2000) 781–790, https://doi.org/10.1016/S0008-8846(00)00239-8.

[10] A. Si Larbi, A. Agbossou, P. Hamelin, Experimental and numerical investigations about textile-reinforced concrete and hybrid solutions for repairing and/or strengthening reinforced concrete beams, Compos. Struct. 99 (2013) 152–162, https://doi.org/10.1016/j.compstruct.2012.12.005.

[11] M.C. Rampini, G. Zani, M. Colombo, M. di Prisco, Mechanical behaviour of TRC composites: experimental and analytical approaches, Appl. Sci. 9 (7) (2019) 1492.

[12] U. Häußler-Combe, J. Hartig, Bond and failure mechanisms of textile reinforced concrete (TRC) under uniaxial tensile loading, Cement Concr. Compos. 29 (4) (2007) 279–289, https://doi.org/10.1016/j.cemconcomp.2006.12.012.

[13] N. Williams Portal, L. Nyholm Thrane, K. Lundgren, Flexural behaviour of textile reinforced concrete composites: experimental and numerical evaluation, Mater. Struct. 50 (1) (2017), https://doi.org/10.1617/s11527-016-0882-9.

[14] A. Romanazzi, D.V. Oliveira, R.A. Silva, An analytical bond stress-slip model for a TRM composite compatible with rammed earth, Construct. Build. Mater. 310 (2021), 125228, https://doi.org/10.1016/j.conbuildmat.2021.125228.

[15] B. Banholzer, Bond of a strand in a cementitious matrix, Mater. Struct. 39 (10) (2006) 1015–1028, https://doi.org/10.1617/s11527-006-9115-y.

[16] E. Lorenz, R. Ortlepp, Bond behavior of textile reinforcements - development of a pull-out test and modeling of the respective bond versus slip relation, in: G. J. Parra-Montesinos, H.W. Reinhardt, A.E. Naaman (Eds.), High Performance Fiber Reinforced Cement Composites 6. RILEM State of the Art Reports, Springer, Dordrecht, 2012.

[17] M. Butler, V. Mechtcherine, S. Hempel, Experimental investigations on the durability of fibre–matrix interfaces in textile-reinforced concrete, Cement Concr. Compos. 31 (4) (2009) 221–231, https://doi.org/10.1016/j.cemconcomp.2009.02.005.

[18] Y. Li, J. Bielak, J. Hegger, R. Chudoba, An incremental inverse analysis procedure for identification of bond-slip laws in composites applied to textile reinforced concrete, Compos. B Eng. 137 (2018) 111–122, https://doi.org/10.1016/j.compositesb.2017.11.014.

[19] N. Williams Portal, I. Fernandez Perez, L. Nyholm Thrane, K. Lundgren, Pull-out of textile reinforcement in concrete, Construct. Build. Mater. 71 (2014) 63–71, https://doi.org/10.1016/j.conbuildmat.2014.08.014.

[20] B. Banholzer, W. Brameshuber, W. Jung, Analytical evaluation of pull-out tests—the inverse problem, Cement Concr. Compos. 28 (6) (2006) 564–571, https://doi.org/10.1016/j.cemconcomp.2006.02.015.

[21] Recommendation of RILEM TC 232-TDT, Test methods and design of textile reinforced concrete, Mater. Struct. 49 (12) (2016) 4923–4927, https://doi.org/10.1617/s11527-016-0839-z.

[22] GOM GmbH, Aramis Adjustable, 2022. https://www.gom.com/en/products/3d-testing/aramis-adjustable. (Accessed 10 February 2022).

[23] GOM GmbH, Gom Correlate, 2022. https://www.gom.com/en/products/gom-suite/gom-correlate-pro. (Accessed 10 February 2022).
[24] SS-EN 12390-3, in: EditionTesting Hardened Concrete - Part 3: Compressive Strength of Test Specimens, vol. 2019, 2019.
[25] DIANA, DIANA Finite Element Analysis, User's Manual, Release 10.5, TNO Building and Construction Research, Delft, Netherlands, 2021.
[26] FIB, CEB-FIP Model Code 2010, Wiley-VCH Verlag GmbH & Co, Lausanne, Switzerland, 2010.
[27] E. Thorenfeldt, A. Tomaszewicz, J.J. Jensen, Mechanical Properties of High-Strength Concrete and Applications in Design, Conference on Utilization of High-Strength Concrete, Stavanger, Norway, 1987.
[28] D.A. Hordijk, Local Approach to Fatigue of Concrete, Delft University of Technology, Delft, Netherlands, 1991.
[29] J.A. Nelder, R. Mead, A simplex method for function minimization, Comput. J. 7 (4) (1965) 308–313, 10.1093/comjnl/7.4.308 %J The Computer Journal.